Thrust and torque production of a squid-inspired swimmer with a bent nozzle for thrust vectoring

Yang Luo[a,b,c], Qing Xiao[c,†], Qiang Zhu[d] and Guang Pan[a,b]

[a]School of Marine Science and Technology, Northwestern Polytechnical University, Xi'an 710072, People's Republic of China

[b]Key Laboratory of Unmanned Underwater Vehicle, Northwestern Polytechnical University, Xi'an, 710072, People's Republic of China

[c]Department of Naval Architecture, Ocean and Marine Engineering, University of Strathclyde, Glasgow, G4 0LZ, United Kingdom

[d]Department of Structural Engineering, University of California San Diego, La Jolla, CA 92093-0085, The United States of America

Abstract

A three-dimensional pulsed-jet propulsion model consisting of a flexible body and a steerable bent nozzle in tethered mode is presented and studied numerically. By prescribing the body deformation and nozzle angle, we examine the flow evolution and propulsive/turning performance via thrust vectoring. Our results show that the vortex ring is no longer axis-symmetric when the jet is ejected at an angle with the incoming flow. A torque peak is observed during jetting, which is mainly sourced from the suction force (negative pressure) at the lower part of the internal nozzle surface when the flow is directed downward through an acute angle. After this crest, the torque is dominated by the positive pressure at the upper part of the internal nozzle surface, especially at a relatively low jet-based Reynolds number ($O(10^2)$). The torque production increases with a larger nozzle bent angle as expected. Meanwhile, the thrust production remains almost unchanged, showing little trade-off between thrust and torque production which demonstrates the advantage of thrust vectoring via a bent nozzle. By decoupling the thrust at the internal and outer surfaces considering special characteristics of force generation by pulsed-jet propulsion, we find that variations in Reynolds number mostly affect the viscous friction at the outer surfaces. The influence of the maximum stroke ratio is also studied. Results show that both the time-averaged thrust and the torque decrease at a larger stroke ratio.

---

† Corresponding author: qing.xiao@strath.ac.uk

1. Introduction

Aquatic animals swim effectively and efficiently, providing numerous prototypes for bio-inspired underwater vehicles. Aquatic locomotion mode can be roughly classified into three main forms, i.e., body/fin undulation, fin oscillation, and jet propulsion. The former two swimming modes have received much attention, and extensive studies have been focused on them in decades (Fish and Lauder, 2006; Fish et al., 2016; Sumikawa et al., 2022; Yu and Huang, 2021; Zhong et al., 2019). In comparison, jet propulsion, utilized by cephalopods such as squid, octopus, and cuttlefish, has gradually attracted interest in recent years due to some inherent merits (Bi and Zhu, 2019b; Gemmell et al., 2021; O'Dor, 2013). Jet propulsion can produce considerable thrust within a split second, which is essential for escape or predation. Some squid are capable of matching the fastest fish when the maximum speed is considered (Gosline and DeMont, 1985). With a turning nozzle, this pulsed jet can also create a notable turning toque for maneuvering in close-quarter environments.

To understand the underlying mechanism of jet propulsion utilized by squid, it is necessary to study the morphology of these animals. The structure of a squid is shown in Fig. 1(a). The mantle, as the main component of a squid, surrounds the mantle cavity (Ward and Wainwright, 1972). Experiments show that the squid mantle has two main muscle types, circular muscles and radial muscles (Thompson and Kier, 2006). According to electromyographic recordings, the radial muscles are active during the hyperinflation of the mantle, while the deflation of the mantle during which the fluid is discharged rapidly is actuated by circular muscles (Gosline et al., 1983), as shown in Fig. 1(b). Ward (1972) found that smooth and uniform changes in diameter (around 15% in moderate jetting) were presented in different parts of the mantle during the inflation-deflation jetting cycle, whereas the mantle length remained almost unchanged.
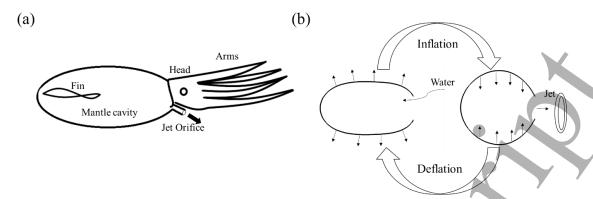
2

Fig. 1. Profile of a squid (a) and the deflation-inflation jetting cycle (b). Reproduced from Fig. 1 in Luo et al. (2020b).

Biological observation and measurement of the hydrodynamics and flow patterns around swimming squid have also been conducted. For example, Anderson and DeMont (2000) evaluated the jet velocity, jet thrust and intramantle pressure based on the measured kinematics, body deformation, and mantle cavity volume of swimming squid (*Loligo pealei*) via high-speed digital video. Similar analyses of squid hydrodynamics were reported by Anderson et al. (2001). Their findings offered new perspectives on the locomotory hydrodynamics of the jetting process of squid and other jet propulsion-based organisms.

Subsequently, DPIV (digital particle image velocimetry) techniques were utilized to visualize the jet flow of squid. Experimental results reported by Anderson and Grosenbaugh (2005) showed that squid jets were periodic, steady, and prolonged emissions of fluid and continuous jets discharged from the squid were unstable. Bartol et al. (2008) found that the jet around squid hatchings (paralarvae) in low and intermediate Reynolds numbers mostly consisted of elongated vortex rings without a clear pinch-off from the trailing tail component. In comparison, the wake patterns of juvenile/adult squid that operate at high Reynolds numbers exhibit two primary jet modes. In jet mode I during slow swimming, the discharged fluid rolls up into a single leading vortex ring at each jet pulse. In jet mode II during fast swimming, the leading vortex ring pinchs off from a long trailing jet with distributed vorticity.

In addition to the jet flow from live squid, vortex ring formation can also be duplicated in experimental environments through a simple piston-cylinder arrangement. Using such a device, Gharib et al. (1998) found that two flow patterns could be produced depending on piston stroke to cylinder diameter ratio (stroke ratio). The flow field at a small stroke ratio shows a single

3

vortex ring, while it consists of a leading vortex ring followed by a trailing wake at a large stroke ratio. These two patterns correspond to the two jet modes I and II observed from live squid, respectively (Bartol et al., 2009). The conversion between these two modes emerges at a specific stroke ratio, the "formation number".

Inspired by the jet-propelled locomotion mode of squid, some robotic designs have been proposed. For example, experiments of a squid-inspired underwater robot named "Robosquid" developed by Moslemi and Krueger (2010) suggested higher propulsive efficiency of the trapezoidal jet velocity profile than the triangular velocity pattern. Nevertheless, the jets were produced by pneumatic or piston actuation rather than inflation-deflation of the body, a key feature of squid jetting. Some squid-inspired soft robotic devices utilized body deformation to produce pulsed jets. An earlier design that combines the concept of soft robotics with pulsed jet production was developed by Serchi et al. (2012). Experiments on this prototype suggested that propulsive performance heavily relied on the flexible response of the robot shell to external actuation. A more recent squid-inspired robot reported by Bujard et al. (2021) demonstrated a preferred Strouhal number for efficient swimming, which is reminiscent of a similar phenomenon in fish swimming.

There are also numerical studies that consider body deformation and jet propulsion of squid-like swimming. By using a potential flow model, Bi and Zhu (2018) investigated the burst-coast swimming of a cephalopod-like jet swimmer. They found that the model could reach optimal swimming speed near the critical stroke ratio. Subsequent studies of a 2D fluid-structure interaction model found symmetry-breaking instability of the jet wake after continuous jetting (Bi and Zhu, 2019b) and the significant role of the added-mass effect in thrust production (Bi and Zhu, 2019a). They also examined the effect of nozzle geometry on jet propulsion performance (Bi and Zhu, 2021a) and jet propulsion efficiency through a novel thrust-drag decomposition (Bi and Zhu, 2021b). The locomotor transition of squid jet from water into air was numerically studied using CFD (computational fluid dynamics) by Hou et al. (2020). They found that a lower launch angle could yield a bigger flying speed. Other numerical studies of jet nozzles can be found in Urazmetov et al. (2021) and Tabatabaei et al. (2015).

4

However, most of the existing studies focused on the thrust production of squid-like jets, while the torque generation, essential for turning or escape maneuvers, receives much less attention. As mentioned earlier, squid achieves "thrust vectoring" by steering its nozzle to a certain angle. Biological measurements indicated that squid exhibited high maneuverability in terms of the lowest length-specific radius of the turn reported for any aquatic taxa (Jastrebsky et al., 2016). Inspired by this feature, a few squid-like robotic designs also showed excellent turning performance. For example, a 3D-printed nozzle with a fixed angle relative to the long axis of a cephalopod-inspired robot made with compliant ribs reached a turning rate up to 50 deg per second (Christianson et al., 2020). Excellent turning maneuverability by cephalopod-inspired soft robots capable of thrust vectoring was also reported by Wang et al. (2019) and Zhang et al. (2020a).

Nevertheless, the above studies focused on mechanical implementation, while the underlying hydrodynamic mechanism remains unrevealed. Although experiments on round jets in cross-flow have been conducted to show the surrounding flow field (Kelso et al., 1996; Lim et al., 2001; New et al., 2006), the thrust and torque created by these transverse jets were not considered in these studies. It is also unclear how the pulsed thrust would change when turning torque is produced by thrust vectoring.

We numerically examine the thrust and torque production of a three-dimensional squid-like swimmer with a bent nozzle in this study. Stemming from a 3D jet propulsor with a pressure chamber and a fixed nozzle in our last work (Luo et al., 2021b), this system is equipped with a steerable nozzle that enables the fluid to be deflected away from the body axis with different angles. A background flow is included to simulate the swimming state before the maneuver. The body deformation is prescribed so that we can examine the effect of the equivalent stroke ratio on the torque generation which has not been studied yet.

The rest of the paper is organized as follows. Section 2 provides the problem statement, including model geometry, deformation design, and performance evaluation method. Then the numerical model and approach are described in section 3. The simulation results are presented in section 4. Finally, section 5 presents the conclusions of this work.

2. Problem statement

The three-dimensional squid-like swimmer considered here consists of a pressure chamber corresponding to the mantle cavity of squid, similar to that in our previous work (Luo et al., 2021b). In addition, a nozzle that mimics the funnel tube is added. This nozzle serves as a fluid exit. For a complete deflation-inflation cycle, when the body cavity deflates, the internal fluid is ejected through the nozzle, then the fluid is absorbed back into the cavity with the body inflating for the next jetting. It is noted that "thrust vectoring" can be achieved by turning the nozzle, which is the key difference between the present model and the previous one in Luo et al. (2021b). In this way, the overall pulsed jet force may not be in line with the direction of the background flow direction and a turning torque will be generated. In this study, only a single deflation phase is considered as it produces most of the thrust and torque during a complete inflation-deflation cycle.

The profile of the squid-like model is presented in Fig. 2(a). The body length is L, the nozzle size is $D = 0.2\,L$ and it has a length of $0.1\,L$. The body geometry and dimension are the same as that in Luo et al. (2021b). Distinctively, a bent nozzle is considered in this work. The bent angle θ of the nozzle is defined as the angle between the axial midlines of the body and the nozzle, as shown in Fig. 2(a). The deflation of the body is achieved by increasing the eccentricity e of an ellipse, while the nozzle is fixed with the given angle θ, as shown in Fig. 2(b). The body length remains unchanged during deformation, consistent with squid jetting jet locomotion (Ward, 1972). The details of the deformation design can be found in Luo et al. (2021b).
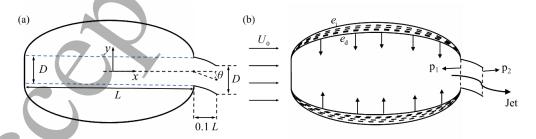

Fig. 2. The profile (a) and deflation (b) of the cross-section of the model (the starting (e_0) and ending (e_1) positions are shown in solid lines). Adapted from Fig. 1 in Luo et al. (2021b). The nozzle inlet and outlet planes are marked as p_1 and p_2, respectively.

6

The deformation of the squid-like model is depicted in Fig. 2. During deflation, the thickness of the wall is varied to keep the volume of the body wall constant to avoid mass change. The initial state, i.e., the inflated state of the body, is denoted by $e = e_i$, while the extreme deflated state is denoted by $e = e_d$. The internal volumes of the body cavity correspond to these two states are $V(e_i)$ and $V(e_d)$, respectively. We define the equivalent stroke ratio as $\Gamma(t) = 4\Lambda(t)/(\pi D^3)$ with $\Lambda(t)= V(e_i) - V(e(t))$ and e denoting the instantaneous eccentricity (Luo et al., 2021b). Then the maximum equivalent stroke ratio, $\Gamma_m = 4(V(e_i) - V(e_d))/(\pi D^3)$ is obtained when the body reaches the fully deflated state. During body shrinking, the spatially-averaged speed $V_j(t)$ around the jet nozzle outlet is given by

$$V_j\left(t\right) = \frac{-4}{\pi D^2}\frac{dV\left(e\right)}{dt} = \frac{d\Gamma}{dt}D. \tag{1}$$

Following Luo et al. (2021b), the jet speed V_j is prescribed as a constant velocity profile, given by

$$V_j(t) = V_{jm}, \ t \in (0, T_d], \tag{2}$$

where V_{jm} is the specified maximum jet speed and T_d denotes the deflation period, given by

$$\int_0^{T_d} V_j\left(t\right)dt = \Gamma_m D. \tag{3}$$

With Eq.(1), we can calculate the instantaneous internal volume $V(e)$ and equivalent stroke ratio $\Gamma(t)$, from which the eccentricity, and thus the body configuration can be obtained. Table I lists the maximum equivalent stroke ratio Γ_m and the corresponding initial eccentricity that we will investigate.

Table I. Γ_m at different e_i with the fully deflated state reached at $e_d = 0.92$ (Luo et al., 2021b).

e_i	0.904	0.898	0.883	0.868	0.844
Γ_m	3.31	4.66	7.60	10.59	15.07

The jet velocity based Reynolds number is calculated by

$$\mathrm{Re}_j = V_{jm}D/\nu, \tag{4}$$

where ν is the kinematic viscosity.

An incoming background flow U_0 is considered to simulate the scenario of sudden turning during steady swimming. The ratio between the incoming flow speed to the jet velocity U_0/V_{jm}

7

is chosen as 0.42, which lies in the range of real squid (Anderson and Grosenbaugh, 2005). This study considers the tethered mode of the model, i.e., it does not swim forward or turn during jetting. Therefore, we define the mean torque coefficient $\overline{C_M}$ acting on the model over one deflation period to evaluate its turning performance as

$$\overline{C_M} = \frac{\frac{1}{T_d}\int_0^{T_d} M(t)\,dt}{0.5\rho V_{jm}^2 D^3}, \tag{5}$$

where $M(t)$ is the torque of the fluidic force on the center of the body, calculated by $M(t) = -\int_{S_b} p(r \times n)\,ds + \int_{S_b} r \times (\tau \cdot n)\,ds$, where S_b denotes the internal and external surface of the model, n denotes the normal vector pointing outward the surface, r is the momentum arm vector, p is pressure, τ is the viscous stress tensor, and the fluid density is denoted by ρ. It is noted that the characteristic speed for normalization is chosen as the jet speed V_{jm} rather than the background flow speed. This is because the vortex ring formation and jet-related thrust production are more associated with V_{jm}.

For this specific study, the nozzle bent angle θ is about the z-axis, as shown in Fig. 2, and therefore, the z-component of the torque coefficient in the xy plane C_{Mz} is our concern, which is defined as

$$C_{Mz}(t) = \frac{M_z(t)}{0.5\rho V_{jm}^2 D^3}. \tag{6}$$

The thrust coefficient C_T and y-direction force coefficient C_y are defined as

$$C_T(t) = -\frac{F_T(t)}{0.5\rho V_{jm}^2 D^2}, \tag{7}$$

and

$$C_y(t) = \frac{F_y(t)}{0.5\rho V_{jm}^2 D^2}, \tag{8}$$

where F_T and F_y are the x and y components of the overall hydrodynamic forces on the swimmer, respectively. The power expenditure coefficient C_P is given by

$$C_P(t) = \frac{P(t)}{0.5\rho V_{jm}^3 D^2}, \tag{9}$$

where P denotes the power consumption of the body calculated by

8

$$P(t) = \iint_{S_b} -(\boldsymbol{\sigma} \cdot \boldsymbol{n}) \boldsymbol{V}_g(t,s) \, ds, \tag{10}$$

where $\boldsymbol{\sigma}$ and $\boldsymbol{V}_g$ represent the stress tensor and velocity vector of the fluid adjacent to the body surface ds, respectively, and $\boldsymbol{n}$ denotes the normal vector.

A turning factor evaluating the torque production performance is defined as

$$\eta_H = \frac{\overline{C_{Mz}}}{\overline{C_P}}, \tag{11}$$

where $\overline{C_P} = \frac{1}{T_d} \int_0^{T_d} C_P(t) \, dt$. The propulsion factor evaluating the propulsion performance is defined as

$$\eta_T = \frac{V_{jm} I}{P_{inp}}, \tag{12}$$

where $I = \int_0^{T_d} -F_x(t) \, dt$ is the overall impulse, and $P_{inp} = \int_0^{T_d} P(t) \, dt$ with P_{inp} denoting the overall energy expenditure during the deflation period (Luo et al., 2021b). The symbols of the physical parameters are summarized in Table II.

Table II. Physical parameters.

C_{Mz}	The torque coefficient in the xy plane	P_{inp}	The overall energy expenditure
C_T	The thrust coefficient	Re	Reynolds number
C_P	The power expenditure coefficient	T_d	The deflation period
C_y	The y-direction force coefficient	U_0	The incoming background flow
e	The eccentricity of an ellipse	V_j	The jet speed at the nozzle
D	The nozzle size	V_{jm}	The maximum jet speed
I	The overall impulse	Γ_m	The maximum equivalent stroke ratio
L	The body length	η_H	The turning factor
$\boldsymbol{M}$	The torque on the center of the body	η_T	The propulsion factor
M_z	The torque in the z-direction	θ	Nozzle bent angle
P	The power consumption	v	The kinematic viscosity

3. Numerical modeling and method

The in-house fluid solver resolves unsteady viscous compressible Navier-Stokes equations which can be written in the integral form as

$$\frac{\partial}{\partial t} \iiint_\Omega \mathbf{U} \, d\Omega + \iint_S (\mathbf{F} - \mathbf{G}) \cdot \mathbf{n} \, dS = 0, \tag{13}$$

9

where **n** is the unit normal vector pointing the outward direction, Ω denotes the fluid domain with boundary S. The conservative state variable is represented by **U**, defined as

$$\mathbf{U} = \{\rho, \rho u, \rho v, \rho w, \rho E\}^{T},\tag{14}$$

where u, v, and w denote the three velocity components in the Cartesian coordinates system, and E represents the total energy of the fluid. The tensor **F** in Eq.(13) is the convective flux and **G** denotes the diffusion flux sourced from the viscous shear stresses.

Using the finite volume method, the fluid domain Ω is divided into a number of hexahedral cells. Each of them is uniquely denoted by (i,j,k), and for one cell, Eq.(13) holds and a semi-discrete form can be derived

$$\frac{\partial}{\partial t}\left(\mathbf{U}_{i,j,k}\Delta\Omega\right)_{i,j,k} - \mathbf{R}_{i,j,k} = \mathbf{J}_{i,j,k},\tag{15}$$

where $\mathbf{U}_{i,j,k}$ is the flow state variable of the cell with the volume of $\Delta\Omega$, $\mathbf{R}_{i,j,k}$ denotes the residual of the net fluxes. $\mathbf{J}_{i,j,k}$ is an artificial viscosity term proposed by Jameson et al. (1981) to stabilize the computation and eliminate non-physical oscillations.

For the time-dependent simulations, a dual-time stepping algorithm is implemented for temporal integration, where Eq.(15) can be reformulated as a steady-state flow problem using a pseudo-time t^{*} (Jameson, 1991)

$$\frac{\partial}{\partial t^{*}}\mathbf{U}^{(n+1)} = \frac{1}{\Delta\Omega}\mathbf{R}^{*}\left(\mathbf{U}^{(n+1)}\right),\tag{16}$$

where

$$\mathbf{R}^{*}\left(\mathbf{U}^{(n+1)}\right) = \mathbf{R}\left(\mathbf{U}^{(n+1)}\right) + \mathbf{J}\left(\mathbf{U}^{(n+1)}\right) - \frac{3\left(\mathbf{U}\Delta\Omega\right)^{(n+1)} - 4\left(\mathbf{U}\Delta\Omega\right)^{(n)} + \left(\mathbf{U}\Delta\Omega\right)^{(n-1)}}{2\Delta t}.\tag{17}$$

A multistage Runge-Kutta scheme is employed to integrate the semi-discrete Eq.(16) to march to convergence in t^{*}. Detailed descriptions of this fluid solver are reported in previous studies (Liu and Ji, 1996; Sadeghi, 2004; Sadeghi et al., 2003).

It is noted that the freestream Mach number, $Ma_0 = U_0/a_0$ where a_0 denotes the sound speed, is chosen as 0.06 to yield negligible compressibility and ensure numerical stability, as we did in our previous simulations (Luo et al., 2021a; Luo et al., 2021b; Shi and Xiao, 2021). The Mach number distribution range is monitored in each simulation to ensure that it is always below the threshold value (0.3) when compressibility becomes pronounced. Moreover, our numerical

10

tests also show that the variation of fluid density is negligible at this freestream Mach number, suggesting the feasibility and accuracy of this fluid solver in solving incompressible flows. In addition, this compressible flow solver has been successfully validated and applied to various incompressible flow simulations associated with boundary movement in our previous work (Liu et al., 2016; Luo et al., 2020a; Shi and Xiao, 2021). The quantitative validations are provided in our previously published papers (Luo et al., 2021a; Luo et al., 2020a; Luo et al., 2020b).

The computational domain and the fluid mesh at the model surface are presented in Fig. 3. The wall condition is applied on the body and nozzle surface, and the non-reflective far-field boundary condition is imposed on the other boundaries (Luo et al., 2021b). A mesh and timestep size independence study is conducted at $Re_j = 1000$, $\theta = 10$ deg, and $\Gamma_m = 10.59$. There are three meshes generated: a coarse mesh with 3.99 million cells, a medium-size mesh with 5.55 million cells, and a fine mesh with 7.77 million cells. The height of the first layer of the three grids is $5 \times 10^{-3} L$. First, three meshes are used with a non-dimensional timestep size, $\overline{\Delta t} = \Delta t V_{jm}/L = 0.025$, to test the mesh convergence, and the results are shown in Fig. 4(a). It is found that the result of the medium-size mesh differs little from that of a fine mesh. Afterward, the influence of the timestep size is also examined by using smaller $\overline{\Delta t}$. It is seen that a smaller timestep size almost does not change the results. Therefore, the following computations are conducted with the medium-size mesh at $\overline{\Delta t} = 0.025$ for computational economy.
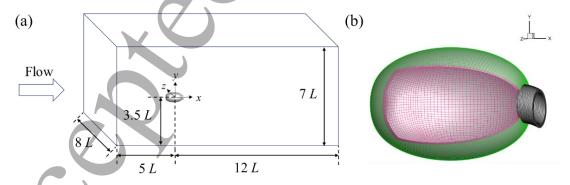

Fig. 3. The layout of the computational domain (not in scale) adapted from Luo et al. (2021b) (a), and the generated fluid mesh at the jet model surface (b). Part of the mesh at the body surface is hidden to show the inner (red), outer (green), and nozzle (black) surface.
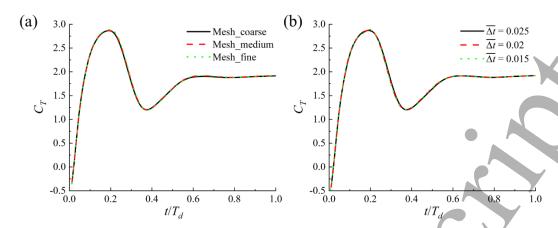
11

Fig. 4. C_T when three meshes are used with $\overline{\Delta t} = 0.025$ (a), and varied timestep sizes are used with the medium-size mesh (b) at Re = 1000, θ = 10 deg and Γ_m = 10.59.

4. Results

The thrust and torque production of a squid-like swimmer via jet through a bent nozzle is numerically studied. Following the previous work (Luo et al., 2021b), the body deflation is started after the external flow field is fully developed, i.e., it becomes quasi-steady.

The bent angle of the nozzle is chosen as 5, 10, and 15 deg. The maximum angle matches the one used by an existing squid-inspired robot by Christianson et al. (2020), which showed that a too large nozzle bent angle only led to spin *in situ*. One demonstration case of a jet swimmer with a bent nozzle is presented to show the propulsion and torque generation. Then a parametric study is conducted to examine the effect of jet-based Reynolds number (Re$_j$ = 100 and Re$_j$ = 1000) and nozzle bent angle, followed by the examination of the effect of the maximum stroke ratio.

4.1 Jet through a bent nozzle

Simulation of the jet propulsion of a squid-like model with a nozzle bent angle θ = 15 deg is performed at Re$_j$ = 1000 and Γ_m = 10.59 in this section. In many previous studies, the jet-propulsion system was often idealized as a piston-cylinder device with a straight tubular nozzle so that the jet is mainly discharged in the axial direction (Abdel-Raouf et al., 2017; Zhang et al., 2020b). In comparison, the present model has a bent nozzle. Thus, it is interesting to see the actual jet profile during the flow passing through the bent nozzle, which is shown in Fig. 5. It

12

is seen that the axial velocity u_x along the body length direction becomes more uniform along the nozzle plane after the jet passes through the nozzle (i.e., two peak speed values become flat) (see Fig. 5(a) and (b)), demonstrating the rectification effect by the nozzle. In addition, we also find that the bent nozzle effectively directs the jet flow as the radial velocity u_y becomes all negative (along the negative y-direction as shown in Fig. 2, downward) after running past it, while the axial speed u_x is generally symmetric about the midline when the jet enters the nozzle. This applies to the early phase of the jetting at $\Gamma = 2.45$. And the radial speed u_y concentrates on the downward nozzle plane, as depicted in Fig. 5(d), at the late phase of the jetting.
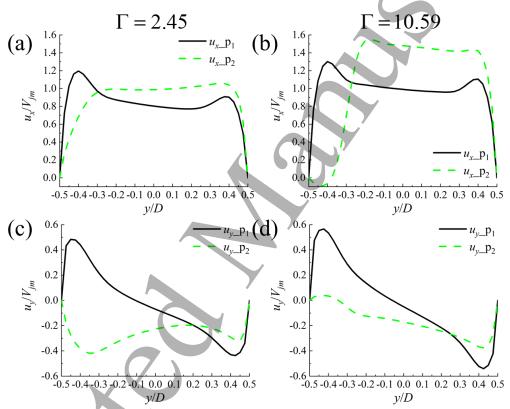
Fig. 5. The axial velocity (u_x) along the body length direction and radial velocity (u_y) along the radial direction (y/D) at the nozzle inlet plane (p_1) and outlet plane (p_2) (see Fig. 2(b)) at $z = 0$ plane at $\Gamma = 2.45$ ((a) and (c)) and $\Gamma = 10.59$ ((b) and (d)) when $Re_j = 1000$, $\theta = 15$ deg, and $\Gamma_m = 10.59$.

To show the surrounding flow field during jetting through a bent nozzle, the Z-vorticity, streamline, and Q criterion distribution at the plane $z = 0$, and iso-surface of Q criterion are presented in Fig. 6. One leading vortex ring followed by distributed vortices is observed herein with the maximum stroke ratio $\Gamma_m = 10.59$ which is larger than 4. Because of the interaction of the background flow and tilted jet about the horizontal midline through a bent nozzle, the wake

13

structure is not symmetric about the horizontal axis, different from that by an axis-symmetric model in previous studies (Bi and Zhu, 2018, 2020; Luo et al., 2021b). This can be seen from the streamline distribution in Fig. 7(a) at $\Gamma = 3.06$, where a stronger vortex is formed near the upper nozzle outlet plane. Thus, the upper part of the vortex ring is better developed at this instant as shown in Fig. 7(b). The upper vortex structure shown by the planar Z-vorticity and Q criterion contour also lasts longer than the lower one which fades quickly after the vortex ring detaches from the nozzle, as depicted in Fig. 6.
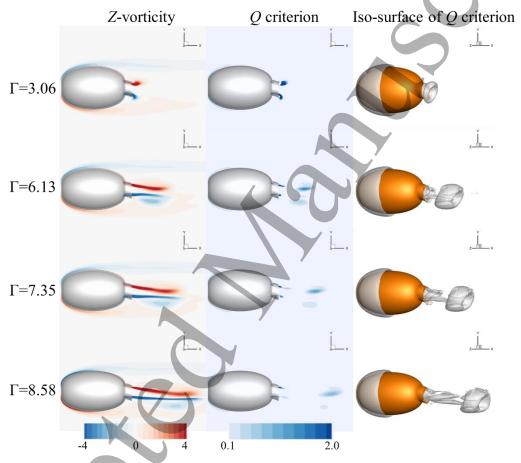
Fig. 6. Z-vorticity and Q criterion distribution at plane $z = 0$, and iso-surface of Q criterion ($Q = 0.05$ after normalization), normalized by V_{jm}/D and $V_{jm}^2 D^2$, respectively, at $\text{Re}_j = 1000$, $\theta = 15$ deg, and $\Gamma_m = 10.59$. The body surface is dyed to facilitate the comparison with the isosurface of the Q-criterion.
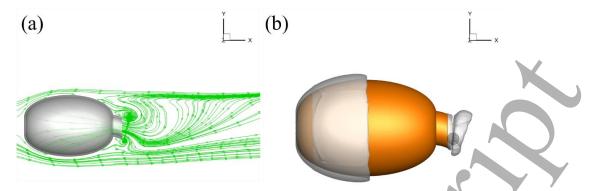
14

Fig. 7. The streamline distribution (a) and iso-surface of Q criterion in xy plane (b) at $\Gamma = 3.06$ when $Re_j = 1000$, $\theta = 15$ deg, and $\Gamma_m = 10.59$.

For insight into the thrust and turning torque production during the jetting, we plot the instantaneous thrust and torque coefficient in Fig. 8. A peak torque value is observed slightly after the maximum thrust, and they both approach a constant during the late phase of the jetting. The thrust generation mechanism has been discussed in our recent work (Luo et al., 2021b). In this work, we focus on torque production. The nozzle is bent downward along the negative y-direction. Therefore, it is reasonable to anticipate that the torque is mainly sourced from the lift force. To this end, we depict the instantaneous lift force coefficient C_y at different parts of the model and compare them with the overall C_y in Fig. 9. It is found that the overall lift force is dominated by the component on the internal nozzle surface. Indeed, by applying the momentum theorem to the jet flow in the y-direction, we expect a vertical reaction force on the internal nozzle surface as the fluid is forced to change flow direction in the bent nozzle. On the other hand, due to the overall asymmetric configuration of the swimmer, the external body surface sustains downward force in the negative y-direction.
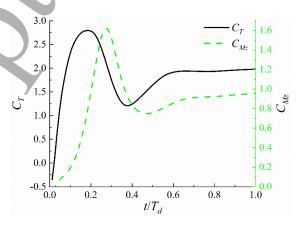

Fig. 8. C_T and C_M in one deflation period at $Re_j = 1000$, $\theta = 15$ deg, and $\Gamma_m = 10.59$.

15

For further insight into the pressure distribution at the internal nozzle surface, the pressure contour is plotted in Fig. 10. As can be seen, the lift force at the internal nozzle surface is mainly sourced from the suction force (negative pressure) at the fore lower surface as the jet flows through an acute angle of the bent nozzle. The positive pressure, mainly located at the rear upper surface, has a smaller magnitude.
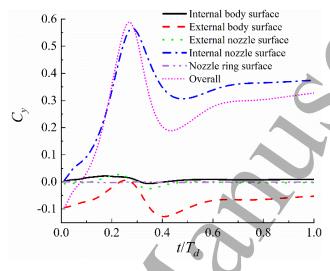

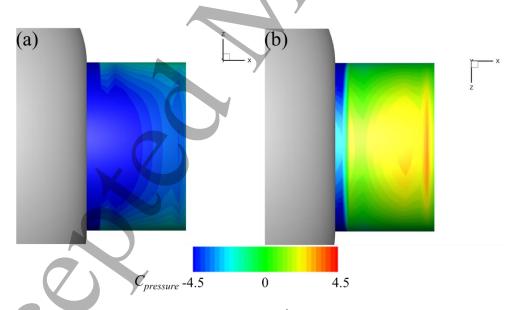Fig. 9. C_y in one deflation period at $Re_j = 1000$, $\theta = 15$ deg, and $\Gamma_m = 10.59$.

Fig. 10. The pressure distributions ($C_{pressure} = p/0.5\rho U_0^2$) on the lower (a) and upper sides (b) of the nozzle internal surface at $\Gamma = 3.06$ ($t = 0.3\ T_d$) when C_y reaches the maximum at $Re_j = 1000$, $\theta = 15$ deg, and $\Gamma_m = 10.59$. The color range is adjusted to reflect the absolute value of pressure to facilitate comparison.

16

It is noted that the flow evolution and force and torque production in realistic free-swimming conditions may be different from the present results in tethered mode. Here, the timescale for rotation is considered to be infinite, and time variation in the external body force is expected to be different for an untethered case. Additionally, if the swimmer could rotate under the torque action relative to the incoming flow, the thrust force may be reduced as the body is less streamlined related to the freestream velocity.

4.2 The effect of nozzle bent angle

In this section, the impact of θ on the thrust and torque production is examined at $Re_j = 100$ and $Re_j = 1000$. The case with a straight nozzle with $\theta = 0$ deg is also included for comparison. Firstly, the axial and radial velocity profiles at the nozzle exit plane with $\theta = 0$ and 15 deg are plotted in Fig. 11 to compare the flow direction through straight and bent nozzles. The bent nozzle breaks the symmetry of these two velocity components about the midline noticeably and the flow is directed downward as expected.
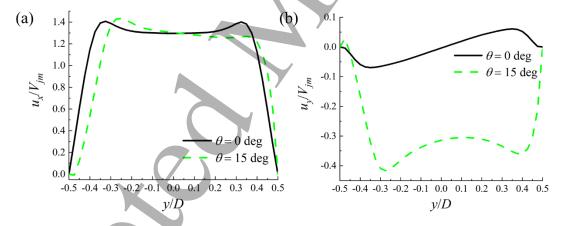

Fig. 11. The speed distribution at the nozzle outlet plane (p2) at $\Gamma = 3.06$ when $Re_j = 1000$ and $\Gamma_m = 10.59$.

To show the effect of this asymmetrical jet flow on force and torque production, Fig. 12 summarizes the performance metrics with two Reynolds numbers. Not surprisingly, the torque production, including the time-averaged and instantaneous torque coefficients, as depicted in Fig. 12(b) and Fig. 13, increases with a larger bent angle of the nozzle. This may be attributed to a larger pressure difference between the upper and lower surfaces of the internal nozzle when

17

flow passes a more acute angle (e.g., see Fig. 10). Nevertheless, the thrust generation that generally remains unchanged with increased θ does not show a trade-off. This is different from the caudal fin propulsion of a sunfish which utilizes different fin movement and deformation patterns to produce thrust and lift force (turning torque). An experiment (Esposito et al., 2012) and numerical simulation of a sunfish-inspired caudal fin (Luo et al., 2020a) suggested that lift force generation via complex tail conformations was usually accompanied by thrust and propulsion efficiency reduction. This does not apply to the "thrust vectoring" of the present squid-inspired jet swimmer which can produce considerable thrust and torque simultaneously, as shown in Fig. 12(a), (b), and (d).
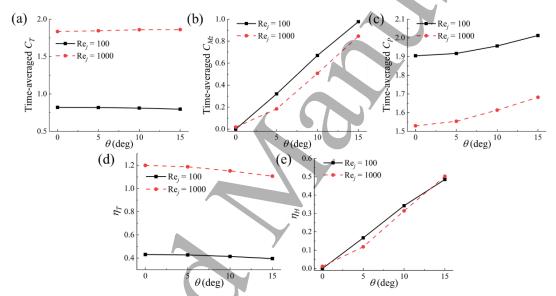

Fig. 12. The mean C_T (a), C_{Mz} (b), C_P (c), η_T (d), and η_H (e) over one deflation period at different nozzle-turning angles.
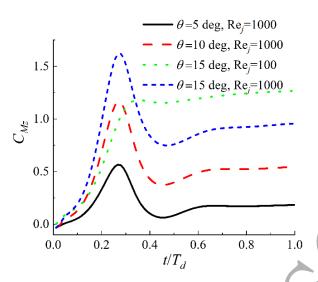
Fig. 13. The comparison of C_{Mz}.

Although the peak torque coefficient is smaller at $Re_j = 100$ compared with that at $Re_j = 1000$ (see Fig. 13), its time-averaged value over one period is larger than the latter, as shown in Fig. 12(b). This is related to the instantaneous torque production profile at the two Reynolds numbers, i.e., the torque at $Re_j = 1000$ decreases significantly during the steady jetting phase after reaching the peak at $t = 0.3\ T_d$. In contrast, at $Re_j = 100$, C_{Mz} maintains a relatively large magnitude after the peak, even larger than the one at $Re_j = 1000$, as presented in Fig. 13. The drop of C_{Mz} at $Re_j = 1000$ after the peak is closely related to the pressure distribution at the internal nozzle surface depicted in Fig. 14. A comparison of Fig. 10 and Fig. 14 shows that the negative pressure at the lower nozzle surface, the main source of the torque production at the maximum C_{Mz}, is reduced significantly in magnitude and distribution area during steady jetting at $Re_j = 1000$. Thus, the torque production is weakened at the steady jetting phase despite that the positive pressure at the upper surface increases slightly. In comparison, the positive pressure with a larger distribution area dominates the upper internal nozzle surface at $Re_j = 100$, along with a slightly smaller negative pressure at the lower surface. In this way, the lift force and therefore, the torque production about the z-axis, at $Re_j = 100$ are expected to be larger than those at the other value of Reynolds number during steady jetting, as seen in Fig. 13.
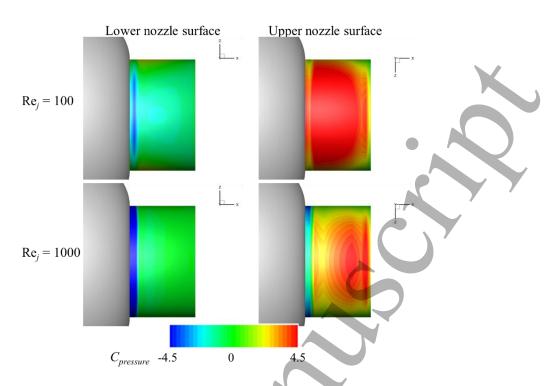
19

Fig. 14. The pressure distributions on the lower and upper sides of the nozzle internal surface at $t = T_d$ with two different Re_j when $\theta = 15$ deg and $\Gamma_m = 10.59$.

The overall thrust C_T is given by the thrust C_x produced by the body deformation minus the drag force C_D, i.e., $C_T = C_x - C_D$. The jet-based Reynolds number and nozzle bent angle have effects on them. We first compare three main thrust sources of C_x identified in our recent work (Luo et al., 2021b) in Fig. 15. They include the thrust coefficient C_{Tj} attributed to jet momentum flux given by

$$C_{Tj} = F_j / \left(0.5\rho V_{jm}^2 D^2\right), \tag{18}$$

where

$$F_j = \int_A \rho u_x^2 dS, \tag{19}$$

where A represents the nozzle plane; the over pressure-related thrust coefficient $C_{Tp} = F_p/(0.5\rho V_{jm}^2 D^2)$ at the nozzle outlet plane with F_p denoting the over-pressure force given by $F_p = \int_A \Delta p dS$ ($\Delta p = p - p_\infty$, where p_∞ is far-field pressure); and the thrust F_m sourced from the temporal variation of the fluid momentum inside the body with a normalized form as $C_{Tm} = F_m/(0.5\rho V_{jm}^2 D^2)$ (Luo et al., 2021b).
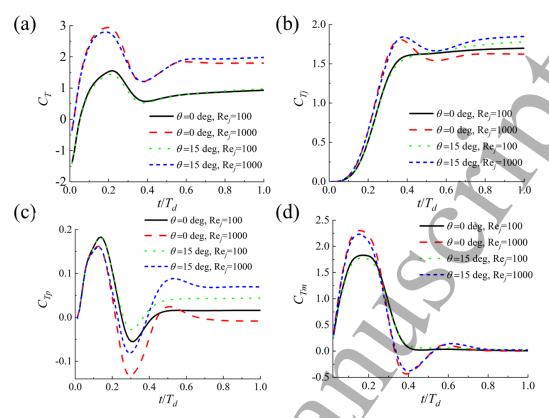
20

Fig. 15. The comparison of overall C_T (a), and three thrust sources, C_{Tj} (b), C_{Tp} (c), and C_{Tm} (d).

In general, the three jet thrust sources are more affected by the jet-based Reynolds number compared with the nozzle bent angle. Especially, the over-pressure-related thrust C_{Tp} shows large differences in terms of relative portion at different jet-based Reynolds numbers and the nozzle-bent angles at the constant jetting phase. For example, the difference in C_{Tp} during the constant jetting phase after $t = 0.6\ T_d$ remains around 150% and 58% at $\theta = 0$ deg and 15 deg from $\mathrm{Re}_j = 100$ to $\mathrm{Re}_j = 1000$, respectively. The effect of θ on C_{Tp} is also significant at the constant jetting phase with the difference in C_{Tp} reaching 174% and 110% at $\mathrm{Re}_j = 100$ and $\mathrm{Re}_j = 1000$ from $\theta = 0$ deg to 15 deg, respectively.

Fig. 16 presents the pressure distribution near the nozzle outlet plane at $t = 0.3\ T_d$. Consistent with the pressure field at the internal nozzle surface, the positive pressure concentrates on the upper nozzle outlet plane when the nozzle is bent, while for a straight nozzle, the exit ring plane is surrounded by negative pressure. This negative pressure has a more dominant influence around the exit plane with a larger Reynolds number, especially at $\theta = 0$ deg, and thus, the minimum C_{Tp} depicted in Fig. 15(c) is seen at this instant for a straight nozzle.
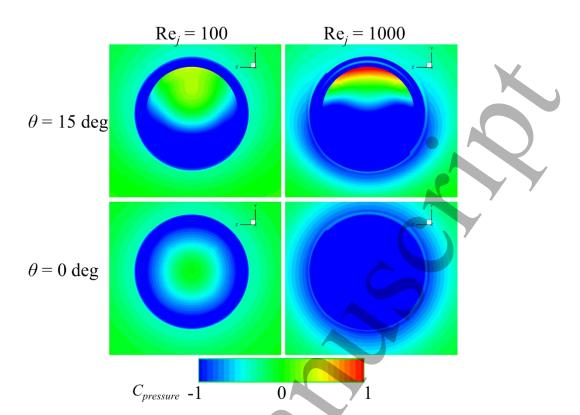
21

Fig. 16. The pressure distribution near the nozzle outlet plane p_2 when C_{Tp} reaches the valley values at $t = 0.3\ T_d$.

The gap between C_T at $\mathrm{Re}_j = 100$ and $\mathrm{Re}_j = 1000$ can not be filled by any single factor of the three thrust sources that include the force generated from the jet wake discussed above. They are just a subset of C_T, and the drag force C_D on the body also plays an important role. This drag force is dominated by viscous drag as the force on the outer surface is directly affected by the background flow (Bi and Zhu, 2021b). Then we can roughly decouple the overall difference in C_T between the cases $\mathrm{Re}_j = 100$ and $\mathrm{Re}_j = 1000$ into two parts, at the internal and outer body surfaces, corresponding to C_x and C_D respectively, in Fig. 17. As can be seen, the force generation on the outer surface contributes the bulk of the discrepancy of overall thrust force at the two different jet-based Reynolds numbers, especially during the constant thrust phase.
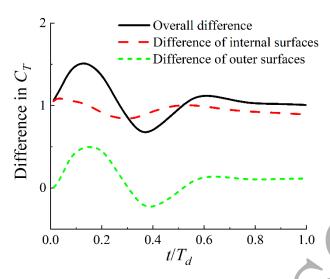
22

Fig. 17. The difference in instantaneous thrust coefficient between the cases $\mathrm{Re}_j=100$ and $\mathrm{Re}_j=1000$ at $\Gamma_m = 10.59$ and $\theta = 15$ deg.

4.3 The effect of stroke ratio

Previous studies of a piston-cylinder arrangement suggested that the wake characteristics of the jet flow were determined by the maximum stoke ratio. Some researchers even argued that the optimal propulsion performance might occur at the formation number (Linden and Turner, 2001). These studies focused on the jet by a straight nozzle in the rest fluid. How the maximum stroke ratio affects thrust and torque production when the nozzle has a bent angle in the presence of background flow remains less known. In this section, its effect is examined by conducting simulations using additional values of Γ_m listed in Table I with $\mathrm{Re}_j = 1000$ and $\theta = 15$ deg.

The streamline, Z-vorticity, Q-criterion distribution at the middle plane $z = 0$, and flow structure when the body is fully deflated at the end of the deflation for the cases with $\Gamma_m = 3.31$ and 10.59 are shown in Fig. 18. At a small Γ_m, the jet flow seems to be fully discharged into the leading vortex ring. When the maximum stroke ratio is increased to 10.59, the wake structure is more complex where the vortex ring is followed by distributed vortices. The vortex rings at the two values of stroke ratios are no longer axial-symmetric, unlike those behind a straight nozzle in our previous study (see Fig. 5 in Luo et al. (2021b)).

For insight into the propulsion and turning capabilities, we plot the performance metrics with varied maximum stroke ratios in Fig. 19. The variation patterns of $\overline{C_T}$ and η_T are generally similar to those of a jet swimmer with a straight nozzle (Bi and Zhu, 2020; Luo et al., 2021b),

i.e., they both decrease as Γ_m goes up. This is partly because a smaller Γ_m corresponds to a less inflated body, thus a smaller drag force. For this reason, the peak instantaneous thrust coefficient C_T and torque coefficient C_{Mz}, as shown in Fig. 20(a) and (b), are increased at a smaller Γ_m. Unlike $\overline{C_T}$, the time-averaged torque coefficient $\overline{C_{Mz}}$ over one deflation period is not sensitive to the variation of maximum stroke ratio. Nevertheless, with the increased power expenditure during jetting at a larger Γ_m as presented by Fig. 20(c), the turning factor η_H goes down correspondingly. The case with $\Gamma_m = 10.59$ and $\theta = 0$ deg, i.e., a straight nozzle, is also included for comparison. It is found that the peak instantaneous thrust of a bent nozzle is smaller than that of a straight nozzle as the fluid may lose some horizontal kinematic energy that accounts for turning torque production when passing a bent nozzle. For a similar reason, the instantaneous power expenditure for a straight nozzle is always lower than the counterparts of a bent nozzle after $t = 0.2\ T_d$ at the same Γ_m.
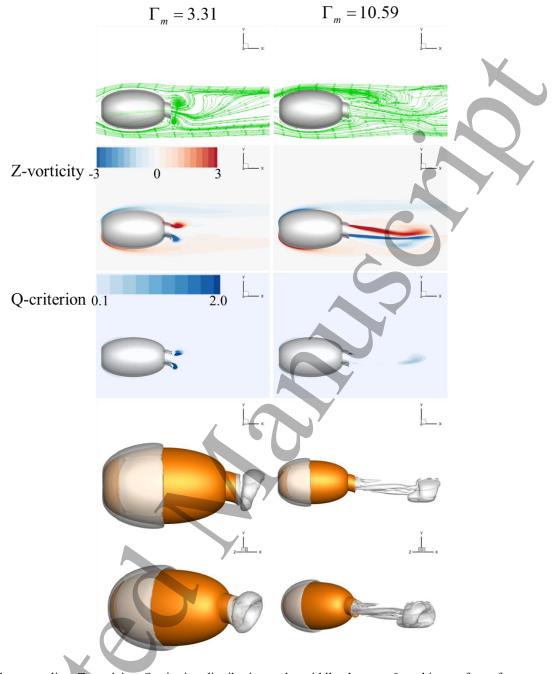
24

$$\Gamma_m = 3.31 \qquad \Gamma_m = 10.59$$

Z-vorticity $-3 \qquad 0 \qquad 3$

Q-criterion $0.1 \qquad 2.0$

Fig. 18. The streamline, Z-vorticity, Q-criterion distribution at the middle plane $z = 0$, and iso-surface of Q-criterion at the end of the deflation for the cases with $\Gamma_m = 3.31$ and 10.59.
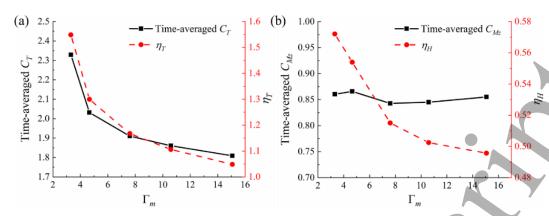
Fig. 19. $\overline{C_T}$, η_T (a), $\overline{C_{Mz}}$, and η_H (b) at different stroke ratios with Re$_j$ = 1000 and θ = 15 deg.
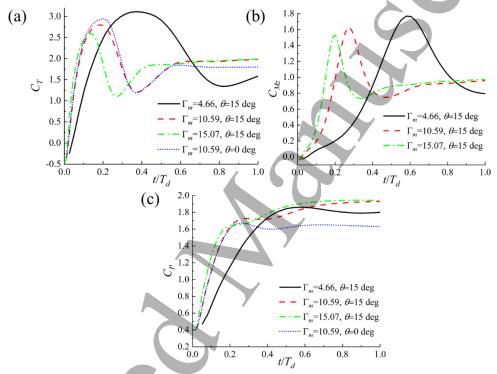

Fig. 20. C_T, C_{Mz}, and C_P in one deflation period at different stroke ratios with Re$_j$ = 1000.

5. Conclusions

The jet propulsion and torque production performance of a squid-like model is numerically studied in this work. This cephalopod-like model has a deformable pressure chamber with a steerable bent nozzle. The chamber deflates by increasing the eccentricity of the body so that the internal flow is ejected with an angle about the midline and background uniform flow. The effects of nozzle bent angle, jet-based Reynolds number, and maximum stroke ratio on the propulsive performance and torque generation are systematically studied.

26

The bent nozzle is proved to be effective in flow rectification and direction, demonstrated by the axial and radial velocity profile at the inlet and outlet nozzle plane. The leading vortex ring discharged from this bent nozzle is no longer axi-symmetrical and its upper part becomes plumper than the lower part. A turning torque about the z-axis in the anticlockwise direction is produced during the jetting in addition to a pulsed thrust force which peaks slightly earlier than the former. By decoupling the lift force associated with this torque at different parts of the model surface, we find the lift force acting on the internal nozzle surface may contribute most to the torque generation. Furthermore, the pressure distribution shows that this force (and the torque) is mainly sourced from the suction force (negative pressure) at the fore lower surface as the jet flows through an acute angle of the bent nozzle.

Our systematic simulations suggest increased torque production at a larger nozzle bent angle as expected. Meanwhile, the thrust production is not reduced with increased torque generation, different from the caudal fin locomotion mode in which turning torque production for maneuvers is usually accompanied by decreased thrust force.

The jet-based Reynolds number affects both the torque and thrust production. Regarding the torque coefficient, although a distinctive peak value of C_{Mz}, attributed to notable negative pressure (suction force) at the lower internal nozzle surface when the nozzle is bent downward relative to the body length direction, is seen during unsteady jetting at a higher Re_j (1000), it decreases significantly after the crest. In comparison, the instantaneous torque coefficient remains at a high level at low Re_j (100) with the upper nozzle surface being dominated by remarkable positive pressure during this steady jetting phase. As a result, its time-averaged torque coefficient is larger than that at a higher Re_j. Our results also show that the jet-based Reynolds number has a significant impact on the over-pressure-related thrust (C_{Tp}) during the constant jetting phase by changing the pressure distribution at the nozzle exit plane. It has little effect on the other two jet-related thrust sources including the thrust sourced from momentum flux (C_{Tj}) and internal fluid momentum variation (C_{Tm}). Considering special characteristics of force generation by pulsed-jet propulsion, we find that the difference in the overall thrust force at the two values of Re_j is mainly dominated by the viscous friction at the outer surfaces by decoupling the thrust at the internal and outer surfaces of the squid-like jet model.

27

The effect of the maximum stroke ratio on torque production is similar to that on the thrust force, i.e., a smaller maximum stroke ratio results in a larger peak and time-averaged torque coefficient. Nevertheless, the turning factor is not as sensitive to the maximum stroke ratio as the propulsion factor is, which shows a continuous decrease with a larger maximum stroke ratio. In this study, the body deformation is prescribed and no material behavior or structural dynamics is considered. Future studies may be focused on a jet model with the structural response being considered in free maneuvering mode to examine the turning radius and velocity in a stationary fluid.

Acknowledgments

Data Availability

The data that support the findings of this study are available from the corresponding author upon reasonable request.

References

Abdel-Raouf, E., Sharif, M.A.R., Baker, J., 2017. Impulsively started, steady and pulsated annular inflows. Fluid Dynamics Research 49, 025511.

Anderson, E.J., DeMont, M.E., 2000. The mechanics of locomotion in the squid Loligo pealei: locomotory function and unsteady hydrodynamics of the jet and intramantle pressure. Journal of Experimental Biology 203, 2851-2863.

Anderson, E.J., Grosenbaugh, M.A., 2005. Jet flow in steadily swimming adult squid. Journal of Experimental Biology 208, 1125-1146.

Anderson, E.J., Quinn, W., De Mont, M.E., 2001. Hydrodynamics of locomotion in the squid Loligo pealei. Journal of Fluid Mechanics 436, 249.

Bartol, I.K., Krueger, P.S., Stewart, W.J., Thompson, J.T., 2009. Hydrodynamics of pulsed jetting in juvenile and adult brief squid Lolliguncula brevis: evidence of multiple jetmodes' and their implications for propulsive efficiency. Journal of Experimental Biology 212, 1889-1903.

28

Bartol, I.K., Krueger, P.S., Thompson, J.T., Stewart, W.J., 2008. Swimming dynamics and propulsive efficiency of squids throughout ontogeny. Integrative and comparative biology 48, 720-733.

Bi, X., Zhu, Q., 2018. Numerical investigation of cephalopod-inspired locomotion with intermittent bursts. Bioinspiration & Biomimetics 13, 056005.

Bi, X., Zhu, Q., 2019a. Dynamics of a squid-inspired swimmer in free swimming. Bioinspiration & Biomimetics 15, 016005.

Bi, X., Zhu, Q., 2019b. Fluid-structure investigation of a squid-inspired swimmer. Physics of Fluids 31, 101901.

Bi, X., Zhu, Q., 2020. Pulsed-jet propulsion via shape deformation of an axisymmetric swimmer. Physics of Fluids 32, 081902.

Bi, X., Zhu, Q., 2021a. Effect of nozzle geometry on the performance of pulsed-jet propulsion at low Reynolds number. Journal of Fluids and Structures 107, 103402.

Bi, X., Zhu, Q., 2021b. Efficiency of pulsed-jet propulsion via thrust-drag decomposition. Physics of Fluids 33, 071902.

Bujard, T., Giorgio-Serchi, F., Weymouth, G., 2021. A resonant squid-inspired robot unlocks biological propulsive efficiency. Science Robotics 6.

Christianson, C., Cui, Y., Ishida, M., Bi, X., Zhu, Q., Pawlak, G., Tolley, M.T., 2020. Cephalopod-inspired robot capable of cyclic jet propulsion through shape change. Bioinspiration & Biomimetics 16, 016014.

Esposito, C.J., Tangorra, J.L., Flammang, B.E., Lauder, G.V., 2012. A robotic fish caudal fin: effects of stiffness and motor program on locomotor performance. The Journal of Experimental Biology 215, 56-67.

Fish, F.E., Lauder, G.V., 2006. Passive and active flow control by swimming fishes and mammals. Annual Review of Fluid Mechanics 38, 193-224.

Fish, F.E., Schreiber, C.M., Moored, K.W., Liu, G., Dong, H., Bart-Smith, H., 2016. Hydrodynamic performance of aquatic flapping: efficiency of underwater flight in the manta. Aerospace 3, 20.

Gemmell, B.J., Dabiri, J.O., Colin, S.P., Costello, J.H., Townsend, J.P., Sutherland, K.R., 2021. Cool your jets: biological jet propulsion in marine invertebrates. Journal of Experimental Biology 224, jeb222083.

Gharib, M., Rambod, E., Shariff, K., 1998. A universal time scale for vortex ring formation. Journal of Fluid Mechanics 360, 121-140.

Gosline, J.M., DeMont, M.E., 1985. Jet-propelled swimming in squids. Scientific American 252, 96-103.

Gosline, J.M., Steeves, J.D., Harman, A.D., Demont, M.E., 1983. Patterns of circular and radial mantle muscle activity in respiration and jetting of the squid Loligo opalescens. Journal of Experimental Biology 104, 97-109.

Hou, T.G., Yang, X.B., Wang, T.M., Liang, J.H., Li, S.W., Fan, Y.B., 2020. Locomotor transition: how squid jet from water to air. Bioinspiration & Biomimetics 15, 036014.

Jameson, A., 1991. Time dependent calculations using multigrid, with applications to unsteady flows past airfoils and wings, 10th Computational Fluid Dynamics Conference. American Institute of Aeronautics and Astronautics.

Jameson, A., Schmidt, W., Turkel, E.L.I., 1981. Numerical solution of the Euler equations by finite volume methods using Runge Kutta time stepping schemes, 14th Fluid and Plasma Dynamics Conference. American Institute of Aeronautics and Astronautics.

Jastrebsky, R.A., Bartol, I.K., Krueger, P.S., 2016. Turning performance in squid and cuttlefish: unique dual-mode, muscular hydrostatic systems. Journal of Experimental Biology 219, 1317-1326.

Kelso, R.M., Lim, T.T., Perry, A.E., 1996. An experimental study of round jets in cross-flow. Journal of Fluid Mechanics 306, 111-144.

Lim, T.T., New, T.H., Luo, S.C., 2001. On the development of large-scale structures of a jet normal to a cross flow. Physics of Fluids 13, 770-775.

Linden, P.F., Turner, J.S., 2001. The formation of'optimal'vortex rings, and the efficiency of propulsion devices. Journal of Fluid Mechanics 427, 61.

Liu, F., Ji, S., 1996. Unsteady flow calculations with a multigrid Navier-Stokes method. AIAA Journal 34, 2047-2053.

Liu, W., Xiao, Q., Zhu, Q., 2016. Passive Flexibility Effect on Oscillating Foil Energy Harvester. AIAA Journal 54, 1172-1187.

Luo, Y., Wright, M., Xiao, Q., Yue, H., Pan, G., 2021a. Fluid-structure interaction analysis on motion control of a self-propelled flexible plate near a rigid body utilizing PD control. Bioinspiration & Biomimetics.

Luo, Y., Xiao, Q., Shi, G., Wen, L., Chen, D., Pan, G., 2020a. A fluid–structure interaction solver for the study on a passively deformed fish fin with non-uniformly distributed stiffness. Journal of Fluids and Structures 92, 102778.

Luo, Y., Xiao, Q., Zhu, Q., Pan, G., 2020b. Pulsed-jet propulsion of a squid-inspired swimmer at high Reynolds number. Physics of Fluids 32, 111901.

Luo, Y., Xiao, Q., Zhu, Q., Pan, G., 2021b. Jet propulsion of a squid-inspired swimmer in the presence of background flow. Physics of Fluids 33, 031909.

Moslemi, A.A., Krueger, P.S., 2010. Propulsive efficiency of a biomorphic pulsed-jet underwater vehicle. Bioinspiration & Biomimetics 5, 036003.

New, T.H., Lim, T.T., Luo, S.C., 2006. Effects of jet velocity profiles on a round jet in cross-flow. Experiments in Fluids 40, 859-875.

O'Dor, R.K., 2013. How squid swim and fly. Canadian journal of zoology 91, 413-419.

Sadeghi, M., 2004. Parallel computation of three-dimensional aeroelastic fluid-structure interaction.

Sadeghi, M., Yang, S., Liu, F., Tsai, H., 2003. Parallel computation of wing flutter with a coupled Navier-Stokes/CSD method, 41st Aerospace Sciences Meeting and Exhibit, p. 1347.

Serchi, F.G., Arienti, A., Laschi, C., 2012. Biomimetic vortex propulsion: toward the new paradigm of soft unmanned underwater vehicles. IEEE/ASME Transactions On Mechatronics 18, 484-493.

Shi, G., Xiao, Q., 2021. Numerical investigation of a bio-inspired underwater robot with skeleton-reinforced undulating fins. European Journal of Mechanics-B/Fluids 87, 75-91.

Sumikawa, H., Naraoka, Y., Fukue, T., Miyoshi, T., 2022. Changes in rays' swimming stability due to the phase difference between left and right pectoral fin movements. Scientific Reports 12, 2362.

Tabatabaei, M.M., Okbaz, A., Olcay, A.B., 2015. Numerical investigation of a longfin inshore squid's flow characteristics. Ocean Engineering 108, 462-470.

Thompson, J.T., Kier, W.M., 2006. Ontogeny of mantle musculature and implications for jet locomotion in oval squid Sepioteuthis lessoniana. Journal of Experimental Biology 209, 433-443.

Urazmetov, O., Cadet, M., Teutsch, R., Antonyuk, S., 2021. Investigation of the flow phenomena in high-pressure water jet nozzles. Chemical Engineering Research and Design 165, 320-332.

Wang, T., Lidtke, A.K., Giorgio-Serchi, F., Weymouth, G.D., 2019. Manoeuvring of an aquatic soft robot using thrust-vectoring, 2019 2nd IEEE International Conference on Soft Robotics (RoboSoft). IEEE, Seoul, Korea (South), pp. 186-191.

Ward, D.V., 1972. Locomotory function of the squid mantle. Journal of Zoology 167, 487-499.

Ward, D.V., Wainwright, S.A., 1972. Locomotory aspects of squid mantle structure. Journal of Zoology 167, 437-449.

Yu, Y.-L., Huang, K.-J., 2021. Scaling law of fish undulatory propulsion. Physics of Fluids 33, 061905.

Zhang, R., Shen, Z., Zhong, H., Tan, J., Hu, Y., Wang, Z., 2020a. A cephalopod-inspired soft-robotic siphon for thrust vectoring and flow rate regulation. Soft Robotics 8, 416-431.

Zhang, X., Wang, J., Wan, D., 2020b. CFD investigations of evolution and propulsion of low speed vortex ring. Ocean Engineering 195, 106687.

Zhong, Q., Dong, H., Quinn, D.B., 2019. How dorsal fin sharpness affects swimming speed and economy. Journal of Fluid Mechanics 878, 370-385.